Journal of Magnetic Resonance 252 (2015) 103–113

Contents lists available at ScienceDirect

Journal of Magnetic Resonance

journal homepage: www.elsevier.com/locate/jmr

Numerical study of a cylinder model of the diffusion MRI signal for neuronal dendrite trees

Dang Van Nguyen [a,c], Denis Grebenkov [b], Denis Le Bihan [c], Jing-Rebecca Li [a,c,*]

[a] INRIA Saclay-Equipe DEFI, CMAP, Ecole Polytechnique, Route de Saclay, 91128 Palaiseau Cedex, France
[b] LPMC, CNRS – Ecole Polytechnique, F-91128 Palaiseau, France
[c] Neurospin, CEA Saclay, F-91191 Gif sur Yvette, France

ARTICLE INFO

Article history:
Received 15 September 2014
Revised 14 January 2015
Available online 28 January 2015

Keywords:
Diffusion MRI
Cylinder model
Neurites
Dendrite trees

ABSTRACT

We study numerically how the neuronal dendrite tree structure can affect the diffusion magnetic resonance imaging (dMRI) signal in brain tissue. For a large set of randomly generated dendrite trees, synthetic dMRI signals are computed and fitted to a cylinder model to estimate the effective longitudinal diffusivity D_L in the direction of neurites. When the dendrite branches are short compared to the diffusion length, D_L depends significantly on the ratio between the average branch length and the diffusion length. In turn, D_L has very weak dependence on the distribution of branch lengths and orientations of a dendrite tree, and the number of branches per node. We conclude that the cylinder model which ignores the connectivity of the dendrite tree, can still be adapted to describe the apparent diffusion coefficient in brain tissue.

1. Introduction

The relation between the complex geometrical structure of brain tissue and the diffusion magnetic resonance imaging (dMRI) signal has yet to be clarified [1–4]. A starting point for many previous works on modeling the dMRI signal in the brain is a relatively simple geometrical model of the tissue. In white matter, bundles of parallel axons (myelinated or not) are usually modeled by cylinders, yielding anisotropic water diffusion. In turn, gray matter contains neuron bodies with axons and randomly oriented dendrites resulting in nearly isotropic diffusion under typical imaging conditions. These constituents and other cells (e.g., astrocytes) are often represented as spheres (or ellipsoids) and cylinders, all embedded in the extra-cellular space. For example, the geometrical model in [5] is a regular lattice of parallel cylinders in which approximate expressions for the apparent diffusion coefficients (ADCs) at long times were derived. In [6], the geometrical model contains prolate ellipsoids (axons) and spheres (glial cells) and water exchange was effectively accounted for by macroscopic terms. In [7] parallel cylinders were used to model axons while water exchange with the extra-cellular space was neglected. In [8], non-monoexponential dMRI signal decay was explained by restricted diffusion in an ensemble of differently oriented cylinders. The model of thick-walled (myelinated) cylindrical tubes (axons) arranged periodically in a regular lattice and immersed in the surrounding medium was used in [9]. In [10,11], another tissue model distinguishing three types of microstructural environment – intra-cellular, extra-cellular, and cerebrospinal fluid compartments – was proposed to account for the neurite orientation dispersion. In this so-called "neurite orientation dispersion and density imaging" (NODDI) model, the intra-cellular signal contribution was obtained for cylinders whose random orientations followed the Watson distribution. The role of water exchange between several "layers" and towards the outer space was studied in [12,13]. Cylinders with spherical bumps were introduced to model neurite beading and to explain experimental findings after ischemic stroke [14]. A general relation between the long-time asymptotic behavior of ADC and the structural disorder of the medium was investigated in [15,16]. Some other theoretical models and concepts of brain dMRI were reviewed in [17].

The original Callaghan's model [18] of infinitely long and uniformly distributed cylinders and its extensions were employed to interpret the dMRI signal in biological tissues [8,19–23]. For instance, the dMRI signal S in brain tissue was often modeled as the sum of two non-exchanging components: the signal S_i from the intra-cellular compartment (dendrites and axons) and the signal S_e from the extra-cellular compartment (modeled as a Gaussian hindered diffusion) [8,20]:

$$S = (1 - v)S_e + vS_i, \tag{1}$$

* Corresponding author at: INRIA Saclay-Equipe DEFI, CMAP, Ecole Polytechnique, Route de Saclay, 91128 Palaiseau Cedex, France.
E-mail address: jingrebecca.li@inria.fr (J.-R. Li).

http://dx.doi.org/10.1016/j.jmr.2015.01.008
1090-7807/

where v is the volume fraction of water associated with the intracellular compartment. Furthermore, axons and dendrite branches were modeled by straight cylinders that are long enough so that the signal from each cylinder is

$$S_{\mathrm{cyl}} \propto \exp\left(-b\left(D_L \cos^2\beta(\mathbf{e},\mathbf{u_g}) + D_T \sin^2\beta(\mathbf{e},\mathbf{u_g})\right)\right), \tag{2}$$

where $\beta(\mathbf{e},\mathbf{u_g})$ is the angle between the cylinder (oriented along the unit vector $\mathbf{e}$) and the unit vector $\mathbf{u_g}$ parallel to the diffusion-encoding gradient $\mathbf{g}$, and D_L and D_T are the effective longitudinal and transverse diffusivities. The b-value is

$$b \equiv \gamma^2|\mathbf{g}|^2 \int_0^{TE} du\left(\int_0^u f(s)ds\right)^2,$$

where $f(s)$ is the effective temporal profile of diffusion-encoding gradient, and TE is the echo time. For a standard Stejskal-Tanner pulsed-gradient spin-echo (PGSE) profile with two rectangular pulses of duration δ separated by diffusion time Δ, $b = \gamma^2|\mathbf{g}|^2\delta^2(\Delta - \delta/3)$ [24]. Integration over the orientation distribution $Q(\theta,\phi)$ of the cylinders yields

$$S_i = \int \exp\left(-b\left(D_L \cos^2\beta(\mathbf{e}_{\theta,\phi},\mathbf{u_g}) + D_T \sin^2\beta(\mathbf{e}_{\theta,\phi},\mathbf{u_g})\right)\right) Q(\theta,\phi)\, d\theta\, d\phi, \tag{3}$$

where the cylinder orientation $\mathbf{e}_{\theta,\phi}$ is described by spherical coordinates (θ,ϕ). The cylinder model was used to fit neurites density v in Eq. (1) and orientation distribution $Q(\theta,\phi)$ in Eq. (3), see [21,22]. Such characterization of neuronal morphology was validated on the digitally reconstructed neurons from the NeuroMorpho.org database [23,25].

In this paper, we perform a numerical study of the quality of the cylinder model of Eqs. (2) and (3) in describing the dMRI signal from dendrite trees. The motivation is that, even neglecting the bending of dendrite branches, the cylinder model does not account for the fact that the dendrite branches are linked to each other in a tree structure and water molecules may be moving to adjacent branches during the diffusion time. We aim to quantify this effect that may become important when the diffusion length,

$$L_{\mathrm{diff}} = \sqrt{2D_0(\Delta + \delta)}, \tag{4}$$

which typically varies between 5 μm and 25 μm, is comparable to or longer than dendrite branch lengths (here D_0 is the intrinsic diffusion coefficient of water). Note that the importance of diffusive exchange between branches of acinar trees on the dMRI signal in lungs was outlined in [26,27].

We make two simplifications in treating the above problem. The first is that we neglect transverse diffusion in the dendrite branches because their diameter is usually less than a micron, i.e., much smaller than their lengths and typical L_{diff}. The second simplification consists in fitting only the apparent diffusion coefficient instead of the full dMRI signal. Expanding Eq. (3) to the first order in b, one gets

$$ADC_0 = D_L \int \cos^2\beta(\mathbf{e}_{\theta,\phi},\mathbf{u_g})\, Q(\theta,\phi)\, d\theta\, d\phi, \tag{5}$$

where D_T was neglected, and the subscript 0 in ADC_0 emphasizes that ADC is computed in the limit $b \to 0$. For an idealized model of infinitely long randomly oriented cylinders, one gets $D_L = D_0$ due to unrestricted diffusion along these cylinders. Since the branches of a dendrite tree are connected and of finite lengths, Eq. (5) is not necessarily valid. We aim therefore at verifying the usefulness of a cylinder model for the analysis of dMRI signals from dendrite trees. For each generated tree, we compute both the integral over angles θ and ϕ from the chosen branch orientation distribution, and ADC_0 from the dMRI signal obtained by solving numerically the Bloch-Torrey equation on the dendrite tree. Repeating this computation for many random realizations of dendrite trees, we define the effective longitudinal diffusivity D_L from a least squares fit. We examine how the value of D_L and the quality of the fit by Eq. (5) are affected by the tree-like structure of neuronal dendrites. In particular, we show the weak dependence of D_L on the branch orientation and length distributions, and the strong dependence on the diffusion time and the average branch length. Both the finiteness of branch lengths and the connectivity of the dendrite tree influence the longitudinal diffusivity.

2. Method

In order to mimic the diversity in shapes and sizes of neuronal dendrite trees, we generate a large sample of randomly constructed trees, choosing the lengths and orientations of the branches from physiologically reasonable ranges for their distributions [28–30]. We emphasize however that our simplified numerical model is not meant to reproduce precisely the complicated architecture of physiological dendrite trees. Our primary goal here is not to capture as accurately as possible various features of the experimental dMRI signal in cortex tissue, but to understand the effect of tree connectivity onto dMRI measurements that was ignored so far. For each generated tree, we fix the principal orientation along the z-axis and distribute branches with a chosen branch orientation distribution $Q_b(\theta,\phi)$ (see below). The ADC_0 of each dendrite tree is extrapolated from the dMRI signal computed numerically by solving the Bloch-Torrey equation on a tree. We study the effect of branch orientations onto the dMRI signal for a single dendrite tree. While a reliable interpretation of the overall dMRI signal in a macroscopic voxel would require the average over many dendrite trees with their own orientation distribution, the analysis is kept at the scale of a single dendrite tree (its extension to multiple trees being straightforward). We detail the procedure in the following subsections.

2.1. Generation of a large sample of dendrite trees

We model a dendrite tree as the union of linked one-dimensional segments that represent the branches of the tree. We denote a one-dimensional dendrite tree embedded in the three-dimensional space by $\mathcal{N} = \bigcup_{k=1}^{\mathcal{K}} \mathcal{T}_k \subset \mathbb{R}^3$, where $\mathcal{K}$ is the number of branches, and $\mathcal{T}_k$ is a branch (a 1D line segment) of length ℓ_k. We consider two types of trees, with regular and random structures. For trees with regular structure, the number of branches per node is fixed. In turn, we use the algorithm in Appendix A to generate dendrite trees with random structure for which the number of branches per node is random but does not exceed the prescribed maximal number $J_{\max}$. In both cases, dendrite trees are forced to grown up along the z-axis by imposing the directionality constraint $0 \leqslant \phi \leqslant \phi_{\max}$ on branch angles ϕ with the z-axis, where $\phi_{\max} \leqslant \pi/2$ is the prescribed directionality parameter that characterizes the dispersion of dendrite branches around the principal direction (z-axis): smaller $\phi_{\max}$ mean stronger alignment of branches with the z-axis. In other words, we choose the branch orientation distribution $Q_b(\theta,\phi)$ to be uniform in the spherical cap of angle $\phi_{\max}$ around the z-axis. Note that $\phi_{\max}$ plays the similar role as the "concentration parameter" κ of the Watson distribution in the NODDI model [10,11].

The sample is characterized by the following parameters:

- the sample size (i.e., the number of trees in a sample), W;
- the maximum number of branches at each tree node, $J_{\max}$;
- the directionality parameter $\phi_{\max}$;
- the number $\mathcal{K}_i$ of branches for i-th tree;
- the distribution of branch lengths.

Fig. 1 illustrates a random dendrite tree generated by the algorithm in Appendix A for the following parameters: $J_{\max}=4, \phi_{\max}=\pi/2, \mathcal{K}=51$, and the branch lengths are chosen randomly with a uniform distribution in the interval $[10\ \mu\text{m}, 100\ \mu\text{m}]$. Since all branch lengths are independent, the empirical mean length is close to $\frac{1}{2}(\ell_{\max}+\ell_{\min})=55\ \mu\text{m}$, while the standard deviation is simply $\sigma_u/\sqrt{\langle\mathcal{K}\rangle}\simeq 4.7\ \mu\text{m}$, where $\sigma_u=(\ell_{\max}-\ell_{\min})/\sqrt{12}$ is the standard deviation for the uniform distribution over $[\ell_{\min},\ell_{\max}]$, and $\langle\mathcal{K}\rangle=30$ is the mean number of branches for this example.

2.2. Synthetic dMRI signal of dendrite trees

Throughout this paper, we focus on the dMRI signal from isolated dendrite trees by ignoring water diffusion in the extra-cellular space. To compute synthetic dMRI signals of the generated dendrite trees, we solve the Bloch-Torrey equation on one-dimensional tree structures. The transverse magnetization $M_k(\mathbf{r},t)$ of water protons satisfies the Bloch-Torrey equation on each branch $\mathcal{T}_k$ of a dendrite tree

$$\frac{\partial}{\partial t}M_k(s,t)=-i\gamma f(t)\,\mathbf{g}\cdot(\mathbf{p}_k+s\mathbf{e}_k)\,M_k(s,t)+D_0\frac{\partial^2}{\partial s^2}M_k(s,t), \tag{6}$$

where we neglected the water exchange with the extra-cellular space, following Refs. [21,22]. Here i is the imaginary unit, $\gamma=2.67513\times10^8\ \text{rad s}^{-1}\,\text{T}^{-1}$ is the gyromagnetic ratio of water proton, and the branch $\mathcal{T}_k$ has the natural parametrization $\mathcal{T}_k=\mathbf{p}_k+s\mathbf{e}_k$, $s\in[0,\ell_k]$, $\mathbf{p}_k$ being the starting point of the segment, and $\mathbf{e}_k$ its orientation. Since we aim to understand the influence of a dendrite tree structure on dephasing of water protons due to their diffusion under gradient pulses, other relaxation mechanisms such as T_1/T_2 relaxation or susceptibility-induced internal gradients are omitted. Although various aspects of diffusion on trees have been thoroughly investigated (see [31–33] and references therein), the effect of gradient pulses and the consequent dMRI signals remain poorly understood.

Two conditions have to be imposed at the tree junctions. The first condition is the continuity of the magnetization:

$$M_k(\ell_k,t)=M_{k'}(0,t), \tag{7}$$

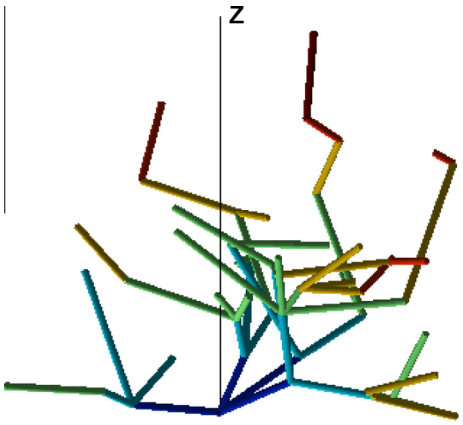

Fig. 1. One random realization of a dendrite tree generated by the algorithm in Appendix A, with $J_{\max}=4, \phi_{\max}=\pi/2, \mathcal{K}=51$, and the branch lengths are chosen randomly with a uniform distribution in the interval $[10\ \mu\text{m}, 100\ \mu\text{m}]$. Although branches are drawn as thick cylinder for visualization, they are treated as infinitely thin segments.

for all $k,k'\in\{1,\dots,\mathcal{K}\}$ such that $\mathbf{p}_{k'}=\mathbf{p}_k+\ell_k\mathbf{e}_k=\mathbf{r}$ (i.e., at the junction $\mathbf{r}$ of branches k and k'). The second condition is the Kirchhoff law ensuring the conservation of flux:

$$\sum_{k:\mathbf{p}_k=\mathbf{r}}\left(\frac{\partial}{\partial s}M_k(s,t)\right)_{s=0}-\sum_{k:\mathbf{p}_k+\ell_k\mathbf{e}_k=\mathbf{r}}\left(\frac{\partial}{\partial s}M_k(s,t)\right)_{s=\ell_k}=0, \tag{8}$$

where the first sum represents outfluxes through branches started at $\mathbf{r}$ (with $\mathbf{p}_k=\mathbf{r}$) while the second sum includes influxes from branches ended at $\mathbf{r}$ (with $\mathbf{p}_k+\ell_k\mathbf{e}_k=\mathbf{r}$). We impose the uniform magnetization as the initial condition:

$$M_k(s,0)=1,\quad k=1,\dots,\mathcal{K}. \tag{9}$$

At the terminal nodes, homogeneous Neumann boundary condition is imposed:

$$D_0\left(\frac{\partial}{\partial s}M_k(s,t)\right)_{s=\ell_k}=0, \tag{10}$$

where $\mathbf{p}_k+\ell_k\mathbf{e}_k$ is the end node of a terminal branch k.

The dMRI signal from the whole dendrite tree is then

$$S(b)\equiv\frac{1}{L}\sum_{k=1}^{\mathcal{K}}\int_{\mathbf{r}\in\mathcal{T}_k}M_k(\mathbf{r},TE)\,d\mathbf{r}, \tag{11}$$

where the total branch length L is

$$L\equiv\sum_{k=1}^{\mathcal{K}}\ell_k=\mathcal{K}\ell_{\text{ave}}.$$

The division by L ensures the conventional normalization of the dMRI signal: $S(0)=1$.

The extrapolated apparent diffusion coefficient

$$ADC_0\equiv-\frac{\partial}{\partial b}\log\frac{S(b)}{S(0)}\bigg|_{b=0}, \tag{12}$$

is calculated numerically by using a cubic polynomial fit of $\log(S(b))$ and taking the coefficient in front of the linear term in b. Defined in this way, ADC_0 exists for arbitrary, not necessarily mono-exponential, dependence of the dMRI signal on b-value. In what follows, we focus on ADC_0 (instead of the dMRI signal) as a source of information about the medium.

2.3. Fitting the cylinder model

For a given dendrite tree, there is only one free fitting parameter in Eq. (5), namely, the longitudinal diffusivity D_L. In other words, since we know exactly the orientations and the lengths of its $\mathcal{K}$ branches, we can rewrite Eq. (5) more explicitly as

$$ADC_0=aD_L \tag{13}$$

with

$$a=\sum_{k=1}^{\mathcal{K}}\frac{\ell_k}{\sum_{j=1}^{\mathcal{K}}\ell_j}\cos^2(\beta_k), \tag{14}$$

where $\beta_k\equiv\mathbf{e}_k\cdot\mathbf{u}_\mathbf{g}$ is the angle between the k-th branch and the diffusion-encoding gradient direction $\mathbf{u}_\mathbf{g}$. Here a is the sample dendrite-weighted mean of $\cos^2(\beta)$ which combines purely geometrical characteristics of a tree and its branch orientations with respect to the gradient direction. Formally, Eq. (13) determines the effective longitudinal diffusivity D_L which *a priori* depends on the whole structure of the dendrite tree. In practice, one aims to infer some geometrical characteristics of dendrites (e.g., the average branch length) from experimentally estimated D_L. Such an inference procedure would be possible if D_L is only sensitive to these averaged characteristics but (almost) independent of the orientation distribution of branches (which is already included in a).

When all branches have the same length, Eq. (14) is reduced to an empirical mean of $\cos^2(\beta)$ over $\mathcal{K}$ independent random realizations of branch orientations. This is a random variable whose mean and standard deviation can be computed analytically for uniform distribution of branch orientations with the directionality constraint $0 \leqslant \phi \leqslant \phi_{\max}$:

$$\langle a\rangle = \frac{1}{2\pi(1-\cos\phi_{\max})}\int_0^{2\pi} d\theta \int_0^{\phi_{\max}} d\phi \sin\phi\cos^2\beta = \frac{2-\cos\phi_{\max}-\cos^2\phi_{\max}+3u_z^2\cos\phi_{\max}(1+\cos\phi_{\max})}{6}, \quad (15)$$

where u_z is the projection of the gradient direction $\mathbf{u_g}$ onto the z-axis, and $\langle\cdots\rangle$ denotes the expectation with respect to the probability distribution of branch orientations. In particular, one retrieves $\langle a\rangle = 1/3$ for both $\phi_{\max} = \pi$ (uniform distribution over the whole sphere) and $\phi_{\max} = \pi/2$ (uniform distribution over the upper hemi-sphere) as expected. In these isotropic cases, the geometrical factor $\langle a\rangle$ does not depend on the gradient direction $\mathbf{u_g}$. In turn, $\langle a\rangle$ does depend on the gradient direction for $\phi_{\max} < \pi/2$. In the extreme case $\phi_{\max} = 0$ when all branches are parallel to the z-axis, one gets $\langle a\rangle = u_z^2$, as expected. One can also compute the standard deviation of a for a tree with $\mathcal{K}$ branches:

$$\mathrm{std}\{a\} = \frac{1}{\sqrt{\mathcal{K}}}\left[\frac{(1-\cos\phi_{\max})^2(17\cos^2\phi_{\max}+41\cos\phi_{\max}+32)}{360} + \cos\phi_{\max}(1-\cos^2\phi_{\max})u_z^2\left(\frac{7\cos\phi_{\max}+5}{12} - u_z^2\frac{5\cos\phi_{\max}+3}{8}\right)\right]^{1/2}. \quad (16)$$

For $\phi_{\max} = \pi$ and $\phi_{\max} = \pi/2$, the standard deviation is equal to $2/\sqrt{45\mathcal{K}}$, while in the limit $\phi_{\max} \to 0$, the standard deviation vanishes, as expected.

2.4. Computational procedure

To investigate the applicability of the cylinder model for inferring geometrical information on dendrite trees from dMRI, we apply the following procedure:

1. Choose the desired form of dendrite trees: regular or random structure, distribution of branch lengths, directionality constraint, distribution of the number of branches, the maximal number of branches per node;
2. Generate a sample of W dendrite trees: $\{\mathcal{N}^1,\ldots,\mathcal{N}^W\}$. The ith tree $\mathcal{N}^i$ has $\mathcal{K}^i$ branches of lengths $\{\ell_k^i\}$ and orientations $\{\mathbf{e}_k^i\}$, $k = 1,\ldots,\mathcal{K}^i$;
3. Determine the factors $\{a_1,\ldots,a_W\}$ for all trees according to Eq. (14);
4. Compute synthetic dMRI signals at eleven b-values spaced between 0 and 500 s/mm^2 for each of the W trees by solving Eqs. (6)–(10) using an adapted version of a finite element method developed in [34];
5. Calculate the associated ADC_0, $\{ADC_0^1,\ldots,ADC_0^W\}$, using a cubic polynomial fit of the logarithm of the signal in b-values;
6. Fit Eq. (13) by solving the least squares problem: finding D_L that minimizes $\sum_{i=1}^W\left(a_i D_L - ADC_0^i\right)^2$, i.e.,

$$D_L = \frac{\sum_{i=1}^W a_i ADC_0^i}{\sum_{i=1}^W a_i^2}. \quad (17)$$

For the chosen form of dendrite trees, this procedure produces the longitudinal diffusivity D_L for a prescribed gradient direction $\mathbf{u_g}$ and sequence timing (δ and Δ). We use the standard PGSE sequence with two rectangular gradient pulses of the fixed pulse duration $\delta = 2.5$ ms and the diffusion time Δ ranging from 2.5 ms to 100 ms.

The intrinsic diffusion coefficient is set to $D_0 = 3\cdot 10^{-3}$ mm^2/s that corresponds to free diffusion of water at 37°C. While higher viscosity and molecular overcrowding in cells can reduce threefold the water diffusion coefficient [35–39], choosing the appropriate value for D_0 in brain tissue is a difficult or even controversial issue. For our purposes, this choice is not critical. In fact, we will show that the ADC_0 mainly depends on the ratio between the average branch length and the diffusion length L_{diff} so that a change in D_0 would simply rescale the diffusion length according to Eq. (4). We will investigate the dependence of the computed D_L on the diffusion time Δ and gradient direction $\mathbf{u_g}$, on one hand, and on various structural features of the dendrite trees, on the other hand.

Beside the best fit D_L, useful quantities associated with the least squares problem are:

(i) the root mean squared fitting error,

$$RMSE \equiv \sqrt{\frac{1}{W}\sum_{i=1}^W\left(a_i D_L - ADC_0^i\right)^2}, \quad (18)$$

(ii) the normalized fitting error,

$$\epsilon_{fit} \equiv \frac{RMSE}{\sqrt{\frac{1}{W}\sum_{i=1}^W\left(ADC_0^i\right)^2}}, \quad (19)$$

and (iii) the scatter ϵ_{D_L} of the best fit D_L,

$$\epsilon_{D_L} \equiv \frac{\sqrt{\frac{1}{W}\sum_{i=1}^W\left(\frac{ADC_0^i}{a_i} - D_L\right)^2}}{D_L}. \quad (20)$$

Note that ϵ_{D_L} characterizes D_L whereas ϵ_{fit} characterizes the ADC_0.

Each simulation was performed for $W = 1000$ random realizations of dendrite trees. We also checked on larger samples with 10,000 trees that both the normalized fitting error ϵ_{fit} and the scatter ϵ_{D_L} reach their limiting values for $W \gtrsim 1000$ (not shown). This verification justifies our choice of the sample size $W = 1000$ which produces statistically representative results.

3. Numerical results

In this section, we investigate how the longitudinal diffusivity D_L depends on various structural features of dendrite trees: branch length (Section 3.1), branch length distribution (Section 3.2), maximal number of branches per node (Section 3.3), directionality constraint (Section 3.4), and gradient direction (Section 3.5). Throughout this section (except for the last subsection), the gradient direction is set to $\mathbf{u_g} = (1,1,1)/\sqrt{3}$. At this gradient direction, the geometrical factor $\langle a\rangle$ from Eq. (15) takes the value 1/3 independently of the directionality constraint $\phi_{\max}$ which by default is set to $\phi_{\max} = \pi/2$ (isotropic case).

3.1. Dependence on diffusion time and branch length

First, we generated $W = 1000$ regular trees with 39 branches ($\mathcal{K} = 39$), spread on three levels: 3 branches at the root, connected to 9 branches on the second level and 27 branches on the third level. The branch lengths, $\ell_1,\ldots,\ell_{39}$ were chosen randomly from an array containing two lengths: 27 μm (30 times) and 90 μm (9 times). Fig. 2 shows the distribution of the simulated ADC_0^i versus the geometrical factors a_i defined in Eq. (14) at $\Delta = 2.5$ ms (Fig. 2(a)), $\Delta = 40$ms (Fig. 2(b)), and $\Delta = 80$ms (Fig. 2(c)). The

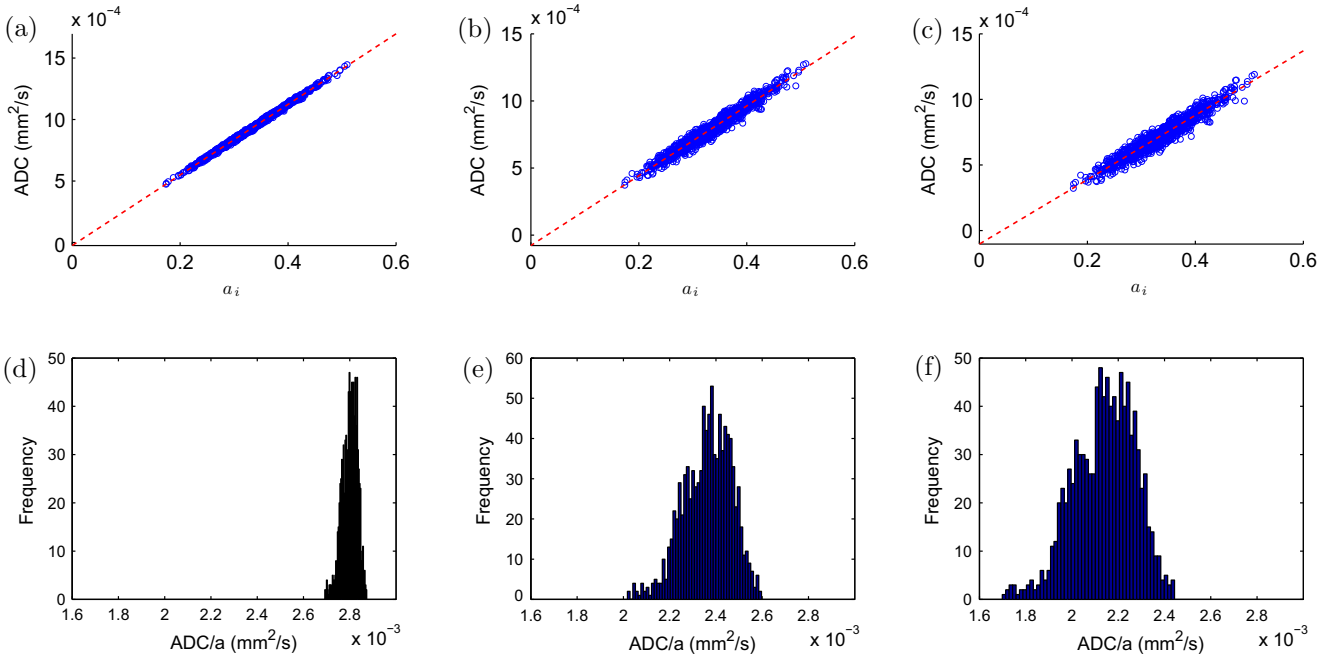

Fig. 2. Distribution of the simulated ADC_0^i versus a_i (defined in Eq. (14)), $i = 1, \ldots, 1000$, at $\Delta = 2.5$ ms (2(a)), $\Delta = 40$ ms (2(b)), $\Delta = 80$ ms (2(c)). The related histograms of the slopes ADC_0^i/a_i at $\Delta = 2.5$ ms (2(d)), $\Delta = 40$ ms (2(e)), $\Delta = 80$ ms (2(f)), with means and standard deviations: $(2.80 \pm 0.03) \cdot 10^{-3}$ mm^2/s, $(2.36 \pm 0.10) \cdot 10^{-3}$ mm^2/s, and $(2.14 \pm 0.13) \cdot 10^{-3}$ mm^2/s, respectively. Simulations were performed on 1000 regular trees, each with $\mathcal{K} = 3 + 9 + 27 = 39$ branches over three levels ($J_{\max} = 4$): 30 branches of length 27 μm and 9 branches of length 90 μm. We set $\phi_{\max} = \pi/2$ and $\mathbf{u_g} = (1, 1, 1)/\sqrt{3}$.

closer the data lie on a straight line, the more accurate the relation Eq. (13) is. Alternatively, one can look on histograms of the slopes ADC_0^i/a_i plotted in Fig. 2(d)–(f) for the three diffusion times. We see clearly that the cylinder model is better at lower diffusion times (the narrowest histogram, with the standard deviation of ADC_0^i/a_i being $0.03 \cdot 10^{-3}$ mm^2/s) and worse at higher diffusion times (the broadest histogram, with the standard deviation of ADC_0^i/a_i being $0.13 \cdot 10^{-3}$ mm^2/s). At $\Delta = 2.5$ ms, the diffusion length $L_{\text{diff}} \simeq 5.5$ μm is much smaller than the branch lengths. At $\Delta = 80$ ms, the diffusion length $L_{\text{diff}} \simeq 22$ μm is on the same order as the length of the shorter set of branches, $\ell = 27$ μm. The normalized fitting errors ϵ_{fit} are 1%, 4%, and 5%, respectively. This level of model error may be considered acceptably low for some applications. The mean values of the ADC_0 for the three diffusion times are: $0.94 \cdot 10^{-3}$ mm^2/s, $0.79 \cdot 10^{-3}$ mm^2/s, and $0.72 \cdot 10^{-3}$ mm^2/s, respectively, while D_L from Eq. (17) are $2.81 \cdot 10^{-3}$ mm^2/s, $2.38 \cdot 10^{-3}$ mm^2/s, and $2.16 \cdot 10^{-3}$ mm^2/s, showing the dependence of D_L on the diffusion time. Note that the ratios between the mean ADC_0 and D_L are close to 1/3, as expected for the isotropic case with $\phi_{\max} = \pi/2$. We emphasize that the above values of the best fit D_L are very close to the sample means of the slope ADC_0^i/a_i: $2.80 \cdot 10^{-3}$ mm^2/s, $2.36 \cdot 10^{-3}$ mm^2/s, and $2.14 \cdot 10^{-3}$ mm^2/s, respectively. In other words, one could introduce the longitudinal diffusivity for each tree as the ratio between ADC_0^i and a_i, and then define D_L as the sample mean of these ratios:

$$D_L' = \sum_{i=1}^{W} \frac{ADC_0^i}{a_i}. \tag{21}$$

Both approaches yield very similar results, and we keep using the best fit D_L from Eq. (17).

The longitudinal diffusivity D_L also depends on the branch length ℓ. When ℓ is long as compared to the diffusion length L_{diff}, most of the water protons remain within one branch and thus dephase at a single gradient strength $|\mathbf{g}| \cos\beta$ (where β is the angle between the gradient direction and that branch orientation). In the limit of infinitely long branches, the nuclei experience the classical dephasing of free one-dimensional diffusion, with D_L being equal to the intrinsic diffusion coefficient D_0. In the opposite short ℓ limit, nuclei are likely to visit several branches during the diffusion time and thus to experience dephasing at various gradient strengths $|\mathbf{g}| \cos\beta_k$. The resulting dMRI signal accounts for switching between branches that yields smaller D_L.

In order to assess the effect of branch length, we generated $W = 1000$ regular trees for which all the branches have the same length ℓ. We simulated 11 values of $\ell : \ell = 10, 15, 20, 30, 35, 40, 45, 55, 70, 100$ μm. As previously, each tree has $\mathcal{K} = 3 + 9 + 27 = 39$ branches on three levels. The results are shown in Fig. 3. One can see that D_L depends on both the branch length ℓ (Fig. 3a) and the diffusion time Δ (Fig. 3c). For example, at $\Delta = 10$ ms, the diffusion length is $L_{\text{diff}} \simeq 8.7$ μm, and $D_L = 1.8 \cdot 10^{-3}$ mm^2/s is much lower than the intrinsic diffusion coefficient $D_0 = 3 \cdot 10^{-3}$ mm^2/s at $\ell = 10$ μm ($\sim L_{\text{diff}}$), while $D_L = 2.75 \cdot 10^{-3}$ mm^2/s is close to D_0 at $\ell = 40$ μm ($\gg L_{\text{diff}}$). In summary, the longitudinal diffusivity D_L deviates significantly from D_0 unless the branch lengths are much longer than the diffusion length. We also see in Fig. 3(b,d) that the scatter of D_L, measured by ϵ_{D_L} from Eq. (20), is smaller when the branch lengths are much longer than the diffusion length, as expected.

The above analysis suggests that the signal and thus the ADC_0 depend on the ratio between the branch length ℓ and the diffusion length L_{diff}. When plotted versus the dimensionless ratio ℓ/L_{diff}, all D_L fall onto one master curve as illustrated in Fig. 3(e). For comparison, we also plotted D_L for a model of randomly oriented disconnected (isolated) branches of length ℓ (see Appendix B). One can see that the connectivity of the dendrite tree plays an important role, i.e., the dependence of D_L on the diffusion time cannot be reduced only to the finiteness of branch lengths. Fig. 3(f) shows that rescaling by the diffusion length is also applicable to ϵ_{D_L}.

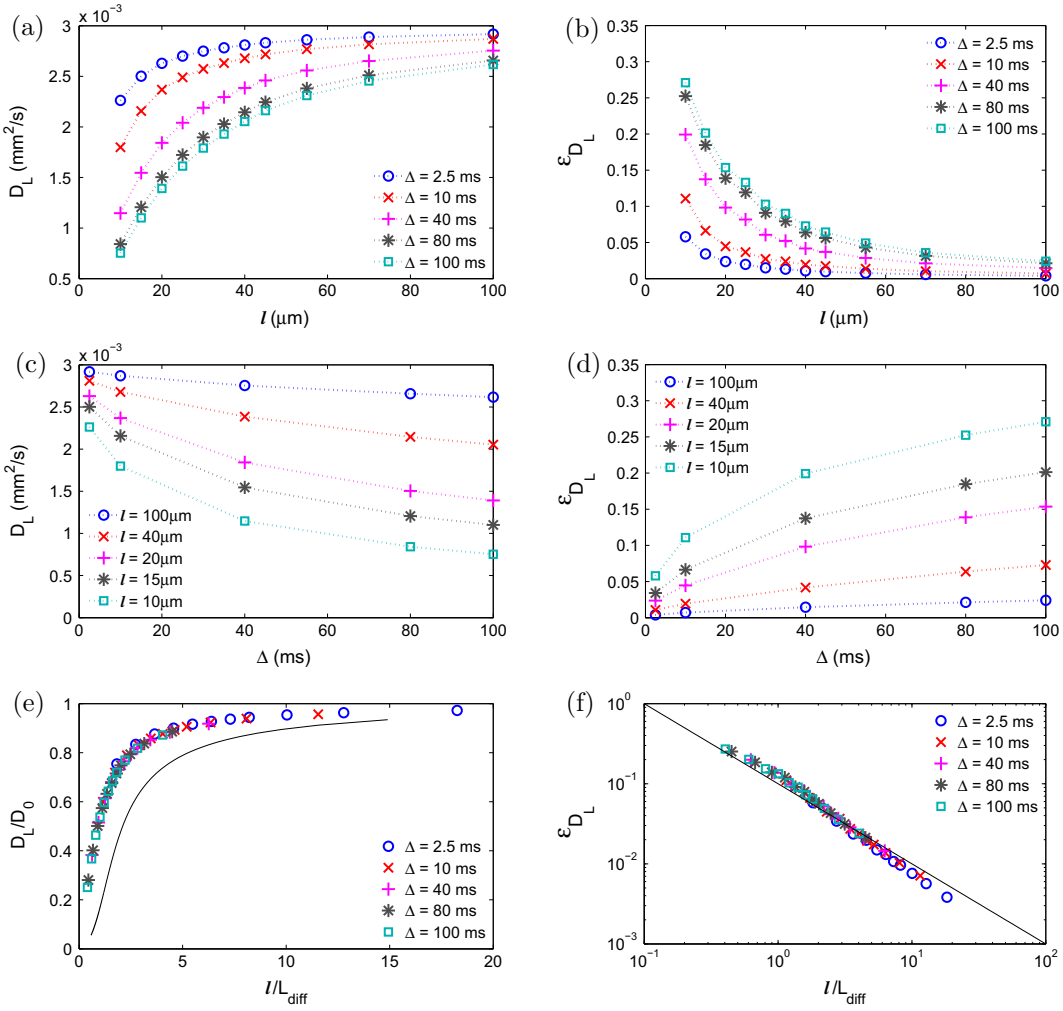

Fig. 3. D_L and ϵ_{D_L} versus branch length ℓ (a, b) and diffusion time Δ (c, d) for dendrite trees for which all the branches have the same length ℓ. When plotted versus the dimensionless ratio $\ell/L_{\rm diff}$, D_L and ϵ_{D_L} fall onto one master curve (e, f). Solid line in Fig. 3(e) shows D_L/D_0 from Eq. (B.2) for a model of disconnected branches. Solid line in Fig. 3(f) indicates the slope -1 in the log–log plot: $0.1(\ell/L_{\rm diff})^{-1}$. Simulations were performed on 1000 regular trees with $\mathcal{K} = 3 + 9 + 27 = 39$ branches over three levels ($J_{\rm max} = 4$), with $\phi_{\rm max} = \pi/2$ and $\mathbf{u}_{\rm g} = (1,1,1)/\sqrt{3}$.

3.2. Little influence of branch length distribution

We compare four samples of $W = 1000$ random trees:

1. For each tree, all the branches have the same length $\ell_{\rm ave}$;
2. For each tree, the branch lengths are chosen randomly from a uniform distribution on the continuous interval $[\ell_{\rm min}, \ell_{\rm max}]$ such that $\ell_{\rm ave} = (\ell_{\rm min} + \ell_{\rm max})/2$;
3. For each tree, the branch lengths are chosen randomly from a Gaussian distribution conditioned to have a prescribed support $[\ell_{\rm min} - \varepsilon, \ell_{\rm max} + \varepsilon]$ (with $\varepsilon > 0$) to avoid negative (or too small) lengths:

$$p_{\rm g}(\ell) = \frac{1}{\mathrm{erf}\left(\frac{L}{\sigma_{\rm g}\sqrt{2}}\right)} \frac{1}{\sqrt{2\pi}\sigma_{\rm g}} \exp\left(-\frac{(\ell - \ell_{\rm ave})^2}{2\sigma_{\rm g}^2}\right),$$

where the first prefactor is the normalization of this conditioned distribution, $\mathrm{erf}(z)$ is the error function, the auxilary parameter ε is fixed to be $\ell_{\rm min}/2, L = \varepsilon + \frac{1}{2}(\ell_{\rm max} - \ell_{\rm min}) = \ell_{\rm max}/2$, and $\sigma_{\rm g}$ is the standard deviation which is matched to the standard deviation of the above uniform distribution, $\sigma_{\rm u} = (\ell_{\rm max} - \ell_{\rm min})/\sqrt{12}$, according to

$$\sigma_u^2 = \sigma_g^2 - 2L\sigma_g \frac{\exp\left(-\frac{L^2}{\sigma_g\sqrt{2}}\right)}{\sqrt{2\pi}\mathrm{erf}\left(\frac{L}{\sigma_g\sqrt{2}}\right)}.$$

4. For each tree, the branch lengths are chosen randomly from a lognormal distribution

$$p_{\rm ln}(\ell) = \frac{1}{\ell\sqrt{2\pi}\sigma_{\rm ln}} \exp\left(-\frac{\left(\ln(\ell/\ell_{\rm ave}) + \sigma_{\rm ln}^2/2\right)^2}{2\sigma_{\rm ln}^2}\right),$$

where $\sigma_{\rm ln}^2 = \ln\left(1 + \sigma_{\rm u}^2/\ell_{\rm ave}^2\right)$.

By construction, all three considered distributions which are fixed by setting $\ell_{\rm min}$ and $\ell_{\rm max}$, have the same mean $\ell_{\rm ave}$ and variance σ_u^2. In all four samples, the number of branches, $\mathcal{K}$, is chosen randomly from a uniform distribution in the set of integers $\{10, 11, \ldots, 50\}$, while the maximal number of branches per node is set to $J_{\rm max} = 4$.

The best fit D_L and the scatter ϵ_{D_L} for the four samples are reported in Table 1 for two choices: $\{\ell_{\rm min} = 10\ \mu\mathrm{m}, \ell_{\rm max} = 100\ \mu\mathrm{m}\}$ and $\{\ell_{\rm min} = 10\ \mu\mathrm{m}, \ell_{\rm max} = 60\ \mu\mathrm{m}\}$. We can see very little difference between D_L and ϵ_{D_L} for all diffusion times between 2.5 ms and 100 ms. We conclude that D_L mainly depends on the

Table 1
Comparison between D_L and ϵ_{D_L} as functions of the diffusion time Δ from the set $\{2.5\text{ ms}, 10\text{ ms}, 40\text{ ms}, 80\text{ ms}, 100\text{ ms}\}$ on four samples of dendrites trees with different branch length distributions: fixed, uniform, conditioned Gaussian, and lognormal, as described in Section 3.2. We set $\ell_{\min} = 10\ \mu$m and consider two choices for $\ell_{\max}$: 60 μm (yielding $\ell_{ave} = 35\ \mu$m) and 100 μm (yielding $\ell_{ave} = 55\ \mu$m). For each sample, simulations were performed on 1000 random trees generated by the algorithm in Appendix A. For each tree, the number of branches $\mathcal{K}$ is randomly chosen between 10 and 50, $J_{\max} = 4$, and we set $\phi_{\max} = \pi/2$ and $\mathbf{u_g} = (1,1,1)/\sqrt{3}$.

ℓ_{ave}	Distrib.	$D_L, \times 10^{-3}$ mm^2/s					Scatter ϵ_{D_L}, %				
		2.5	10	40	80	100	2.5	10	40	80	100
35 μm	Fixed	2.78	2.63	2.30	2.03	1.93	1.3	2.4	5.2	7.9	9.0
	Uniform	2.78	2.64	2.32	2.08	1.99	1.7	3.0	5.9	8.3	9.2
	Gaussian	2.79	2.64	2.33	2.09	2.00	1.6	2.8	5.7	8.1	9.0
	Lognormal	2.78	2.63	2.31	2.06	1.97	1.6	2.9	6.1	8.8	9.8
55 μm	Fixed	2.86	2.77	2.56	2.38	2.31	0.8	1.4	3.0	4.5	5.2
	Uniform	2.86	2.77	2.57	2.40	2.34	1.0	1.8	3.6	5.1	5.7
	Gaussian	2.86	2.77	2.57	2.40	2.34	1.0	1.8	3.6	5.0	5.5
	Lognormal	2.86	2.77	2.56	2.39	2.32	1.0	1.9	3.9	5.6	6.3

average branch length of the dendrite tree, and it is not significantly affected by the specific distribution of branch lengths.

3.3. Little effect of the maximal number of branches per node

We also study the effect of the maximal number of branches per node. We fixed the branch length to be $\ell = 10\ \mu$m, and generated two samples of $W = 1000$ regular trees: in the first sample, each tree has $\mathcal{K} = 3 + 9 + 27 = 39$ branches over three levels ($J_{\max} = 4$), while in the second sample, each tree has $\mathcal{K} = 4 + 16 + 64 = 84$ branches over three levels ($J_{\max} = 5$). Table 2 summarizes the values of D_L and ϵ_{D_L} for broad range of diffusion times. One can see that there is no significant difference in the longitudinal diffusivity D_L between the two samples, though the values of D_L for $J_{\max} = 4$ are systematically greater than that for $J_{\max} = 5$. Note also that the scatter ϵ_{D_L} grows with the diffusion times. A similar comparison has also been performed for random trees when the total number of branches and the number of branches per node are random (the latter being limited by $J_{\max}$). In this case, the D_L are even closer for the two cases $J_{\max} = 4$ and $J_{\max} = 5$ (data not shown). In fact, most of nodes do not attain the maximal number of branches per node so that two samples are closer in this case. We also checked that the effect of $J_{\max}$ is diminished even further for longer branches as the nuclei would move less frequently between branches (checked for $\ell = 55\ \mu$m, data not shown).

3.4. Directionality constraint (branch orientation distribution)

We now look at the effect of the branch orientation distribution. We recall that the angles ϕ the branches make with the z-axis is limited to $\phi_{\max} : 0 \leqslant \phi \leqslant \phi_{\max}$. We generate three samples of $W = 1000$ trees for three values of $\phi_{\max} : \phi_{\max} = \pi/2$, $\phi_{\max} = \pi/6, \phi_{\max} = \pi/12$. In other words, we limited the branch orientations to an increasingly smaller area around the North pole of the unit sphere. The branch lengths were fixed to be $\ell = 55\ \mu$m,$J_{\max} = 4$, and $\mathcal{K}$ is randomly chosen between 10 and 50 for each tree. Fig. 4 shows that the empirical distributions of the geometrical factor a defined in Eq. (14) for the three cases are different. In turn, the empirical means of a $(0.337, 0.337, 0.335)$ are close to the theoretical value $\langle a\rangle = 1/3$ at the chosen gradient direction $\mathbf{u_g} = (1,1,1)/\sqrt{3}$. This observation confirms that the number of branches in simulated trees is sufficiently large to make a discrete sampling representative. We emphasize that the value 1/3 here is not universal as $\langle a\rangle$ would depend on the gradient direction for $\phi_{\max} < \pi/2$ (see below). Note that the same value $\langle a\rangle = 1/3$ for the isotropic case (with $\phi_{\max} = \pi/2$) is independent of the gradient, in which case the classical relation $ADC_0 = D_L/3$ is retrieved. The standard deviations of a_i are $0.06, 0.04, 0.02$, respectively, in agreement with Eq. (16), if the mean $\langle\mathcal{K}\rangle = 30$ is substituted for the number of branches.

We also computed D_L and ϵ_{D_L} for each of the above three values of $\phi_{\max}$. Fig. 5 shows that the relative difference between D_L for these three cases is small (in fact below 5%). The scatter is larger when $\phi_{\max}$ is larger, but ϵ_{D_L} is no more than 5% even at the longest diffusion time $\Delta = 100$ ms. One can conclude that the effect of directionality constraint on the longitudinal diffusivity is minor.

3.5. Effect of gradient direction

To observe the effect of diffusion-encoding gradient direction on D_L and ϵ_{D_L}, we consider one previous sample of 1000 random trees with $\phi_{\max} = \pi/6$ and set three gradient directions: $\mathbf{u_g} = (1,0,\sqrt{3})/2, \mathbf{u_g} = (1,0,1)/\sqrt{2}, \mathbf{u_g} = (\sqrt{3},0,1)/2$. Fig. 6 illustrates a small difference between D_L for the three gradient directions and diffusion times between 2.5 ms and 100 ms.

Numerical results for some other directionality constraints $\phi_{\max}$ and several gradients directions $\mathbf{u_g}$ are summarized in Table 3. The empirical means and standard deviations of a_i and ADC_0^i were computed by averaging over 1000 random trees with $\ell = 55\ \mu$m,$J_{\max} = 4$, and $\mathcal{K}$ is randomly chosen between 10 and 50 for each tree. One can easily check that, for all $\phi_{\max}$ and $\mathbf{u_g}$, the empirical means and standard deviations of a_i are close to their

Table 2
Comparison between D_L and ϵ_{D_L} as functions of the diffusion time Δ from the set $\{2.5\text{ ms}, 10\text{ ms}, 40\text{ ms}, 80\text{ ms}, 100\text{ ms}\}$ on two samples of 1000 regular trees. In the first sample, each tree has $\mathcal{K} = 3 + 9 + 27 = 39$ branches over three levels ($J_{\max} = 4$), while in the second sample, each tree has $\mathcal{K} = 4 + 16 + 64 = 84$ branches over three levels ($J_{\max} = 5$). We set $\ell = 10\ \mu$m or $\ell = 55\ \mu$m, $\phi_{\max} = \pi/2$ and $\mathbf{u_g} = (1,1,1)/\sqrt{3}$.

ℓ	$J_{\max}$	$D_L, \times 10^{-3}$ mm^2/s					Scatter ϵ_{D_L}, %				
		2.5	10	40	80	100	2.5	10	40	80	100
10 μm	4	2.20	1.70	0.99	0.68	0.60	4.1	7.7	13	18	20
	5	2.17	1.65	0.92	0.62	0.55	2.8	5.2	9.1	13	14
55 μm	4	2.85	2.75	2.53	2.34	2.26	0.6	1.0	2.1	3.2	3.6
	5	2.85	2.74	2.51	2.32	2.24	0.4	0.7	1.5	2.2	2.6

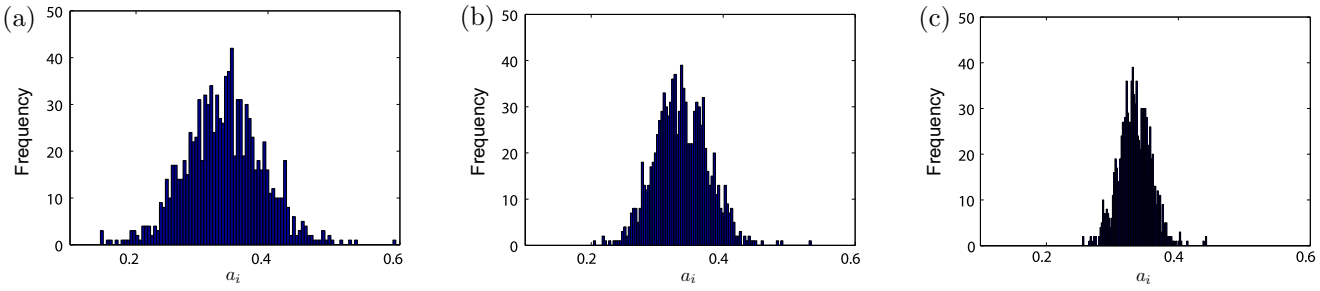

Fig. 4. Distribution of a_i for three choices of $\phi_{\max}$: (a) $\phi_{\max} = \pi/2$, empirical mean and standard deviation of a_i are 0.337 and 0.06, (b) $\phi_{\max} = \pi/6$, empirical mean and standard deviation of a_i are 0.337 and 0.04 and (c) $\phi_{\max} = \pi/12$, empirical mean and standard deviation of a_i are 0.335 and 0.02. Simulations were performed on 1000 random trees with branches of the same length $\ell = 55$ μm, $\mathbf{u_g} = (1,1,1)/\sqrt{3}$, $J_{\max} = 4$, and $\mathcal{K}$ is randomly chosen between 10 and 50 for each tree.

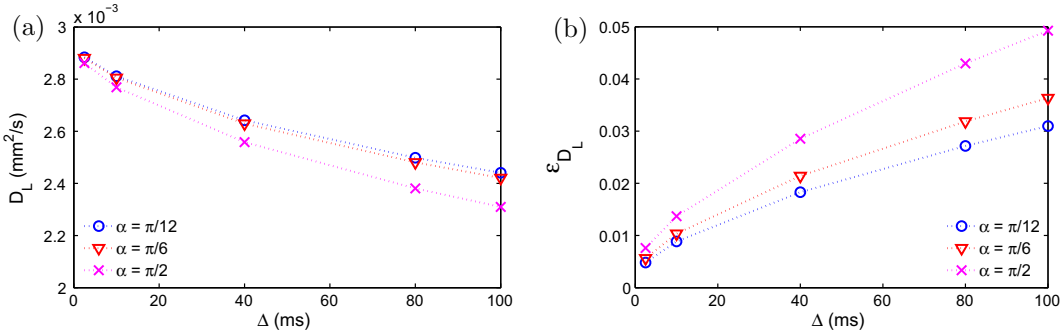

Fig. 5. D_L (a) and ϵ_{D_L} (b) for three directionality constraints $\phi_{\max}$. Simulations were performed on 1000 random trees with branches of the same length $\ell = 55$ μm, $\mathbf{u_g} = (1,1,1)/\sqrt{3}$, $J_{\max} = 4$, and $\mathcal{K}$ is randomly chosen between 10 and 50 for each tree.

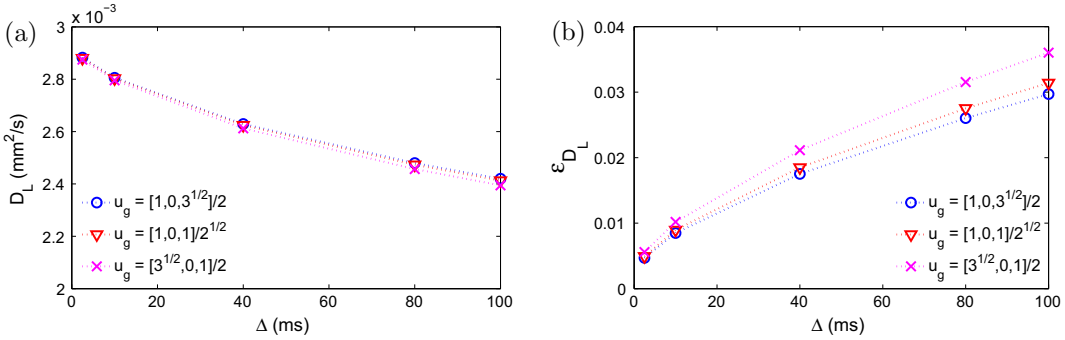

Fig. 6. D_L (a) and ϵ_{D_L} (b) for three gradient directions $\mathbf{u_g} = (1,0,\sqrt{3})/2, \mathbf{u_g} = (1,0,1)/\sqrt{2}, \mathbf{u_g} = (\sqrt{3},0,1)/2$. Simulations were performed on 1000 random trees with branches of the same length $\ell = 55$ μm, $\phi_{\max} = \pi/6$, $J_{\max} = 4$, and $\mathcal{K}$ is randomly chosen between 10 and 50 for each tree.

theoretical values $\langle a \rangle$ and std$\{a\}$ given by Eqs. (15) and (16), respectively. As expected, a_i and ADC_0^i are independent of the gradient direction for the isotropic case with $\phi_{\max} = \pi/2$. In general, ADC_0^i are slightly smaller at the longer diffusion time $\Delta = 80$ ms. Note also that the ratio between the empirical means of ADC_0^i and a_i may be different from the best fit D_L from Eq. (17) due to correlations between ADC_0^i and a_i.

4. Discussion

In the idealized limit of infinitely short gradient pulses (i.e., the double limit $\delta \to 0$ and $g \to \infty$ with b-value being fixed), ADC_0 from Eq. (12) becomes

$$ADC_0 = \frac{1}{2\Delta}\langle[(\mathbf{r}_\Delta - \mathbf{r}_0)\cdot\mathbf{u_g}]^2\rangle, \tag{22}$$

where the average is taken over all starting points $\mathbf{r}_0$ and arrival points $\mathbf{r}_\Delta$ in a confining domain [18]. This is the mean square displacement along the gradient direction $\mathbf{u_g}$, i.e., a purely diffusive characteristics of the medium. When the gradient pulses are not instantaneous, ADC_0 is in general affected by dMRI measurement features such as, e.g., the gradient temporal profile [3]. Throughout this paper, the gradient pulse duration δ was fixed to be 2.5 ms which is representative for brain dMRI. During each gradient pulse, water molecules move on average 3–4 μm so that such δ is not considered to be instantaneous.

The linear relation (13) between ADC_0 and D_L constitutes a simple way to translate a dMRI measurement (ADC) depending on the experimental setup (e.g., the PGSE sequence timing) into a purely diffusive characteristics (D_L) of a confining medium. This quantity characterizes an effective slowing down of diffusion by confinement during the diffusion time Δ. For a valid "translation", the longitudinal diffusivity D_L should be disentangled from dMRI, i.e., be

Table 3
Empirical means and standard deviations of a_i and ADC_0^i for $\Delta = 40$ ms and $\Delta = 80$ ms at three directionality constraints ϕ_{max} and five gradient directions: $\mathbf{u}_g^{(1)} = (1,0,\sqrt{3})/2, \mathbf{u}_g^{(2)} = (1,0,0), \mathbf{u}_g^{(3)} = (1,0,1)/\sqrt{2}, \mathbf{u}_g^{(4)} = (\sqrt{3},0,1)/2, \mathbf{u}_g^{(5)} = (1,1,1)/\sqrt{3}$. Simulations were performed on 1000 random trees with branches of the same length $\ell = 55$ μm, $J_{max} = 4$ and $\mathcal{K}$ is randomly chosen between 10 and 50 for each tree. The empirical mean and standard deviation of a_i are in excellent agreement with the theoretical formulas (15) and (16), when $\mathcal{K} = 30$ is used as the mean value of $\mathcal{K}$.

	$\mathbf{u}_g$	$\phi_{max} = \pi/6$	$\phi_{max} = \pi/3$	$\phi_{max} = \pi/2$
a_i	$\mathbf{u}_g^{(1)}$	0.67 ± 0.04	0.49 ± 0.06	0.33 ± 0.06
	$\mathbf{u}_g^{(2)}$	0.06 ± 0.01	0.21 ± 0.04	0.34 ± 0.06
	$\mathbf{u}_g^{(3)}$	0.47 ± 0.05	0.40 ± 0.07	0.33 ± 0.06
	$\mathbf{u}_g^{(4)}$	0.27 ± 0.04	0.30 ± 0.06	0.34 ± 0.06
	$\mathbf{u}_g^{(5)}$	0.33 ± 0.04	0.34 ± 0.06	0.33 ± 0.06
ADC_0^i, $\times 10^{-3}$ mm^2/s $\Delta = 40$ ms	$\mathbf{u}_g^{(1)}$	1.8 ± 0.11	1.3 ± 0.16	0.86 ± 0.16
	$\mathbf{u}_g^{(2)}$	0.16 ± 0.03	0.53 ± 0.10	0.85 ± 0.15
	$\mathbf{u}_g^{(3)}$	1.2 ± 0.12	1.0 ± 0.17	0.86 ± 0.16
	$\mathbf{u}_g^{(4)}$	0.69 ± 0.11	0.78 ± 0.16	0.85 ± 0.16
	$\mathbf{u}_g^{(5)}$	0.87 ± 0.12	0.87 ± 0.17	0.85 ± 0.16
ADC_0^i, $\times 10^{-3}$ mm^2/s $\Delta = 80$ ms	$\mathbf{u}_g^{(1)}$	1.7 ± 0.11	1.2 ± 0.16	0.81 ± 0.15
	$\mathbf{u}_g^{(2)}$	0.15 ± 0.03	0.49 ± 0.10	0.78 ± 0.15
	$\mathbf{u}_g^{(3)}$	1.2 ± 0.12	0.97 ± 0.17	0.80 ± 0.15
	$\mathbf{u}_g^{(4)}$	0.65 ± 0.10	0.73 ± 0.15	0.79 ± 0.15
	$\mathbf{u}_g^{(5)}$	0.82 ± 0.11	0.81 ± 0.16	0.79 ± 0.15

independent of measurement features. In turn, the proportionality coefficient a in Eq. (13) captures the gradient direction.

The Callaghan's model of uniformly distributed cylinders and its extensions were often employed to describe the dMRI signal in biological tissues [8,18–23]. If the width of cylinders is negligible as compared to the diffusion length, the ADC_0 is simply one third of the longitudinal diffusivity D_L. In this isotropic case, the estimated ADC_0 is evidently independent of the gradient direction and is close to $D_0/3$ for long enough cylinders. In this paper, we investigated the effect of tree connectivity onto the dMRI signal which was ignored so far. A simple model of random dendrite trees grown up along one preferred direction was introduced in order to get statistically representative results. For this purpose, the branch orientations were chosen uniformly over a spherical cap around the North pole (the z-axis) with the directionality constraint $0 \leqslant \phi \leqslant \phi_{max} \leqslant \pi/2$. The maximal angle ϕ_{max} can be varied from $\pi/2$ (upper hemi-sphere) to 0 (all branches are parallel to the z-axis). We aimed to verify the usefulness of the ADC_0 as a source of information about dendrite trees.

We showed that the coefficients a_i for randomly generated trees exhibit a relatively narrow distribution around the mean value $\langle a \rangle$ for which an explicit formula is obtained. In fact, if branch orientations in a tree are independent, the standard deviation of a decreases as $1/\sqrt{\mathcal{K}}$ with the number of branches $\mathcal{K}$. As a consequence, for large dendrite trees, the random coefficient a_i is not spread much and is close to the mean value. In principle, one can measure the dMRI signal along multiple gradient directions in order to get even better estimate of a_i.

Our numerical results show that, unless the branch lengths are much longer than the diffusion length L_{diff}, the longitudinal diffusivity D_L depends significantly on the ratio between the average branch length of a dendrite tree and the diffusion length (the latter being controlled in experiments through the diffusion time Δ). In contrast to an idealized model of infinitely long cylinders (for which $D_L = D_0$), the dependence of D_L on the diffusion time is caused by the finiteness of branch lengths and by the connectivity of the dendrite tree. Both effects are significant because a simplified model of disconnected branches of finite lengths which ignores the connectivity (see Appendix B), underestimates D_L as illustrated on Fig. 3(e). On one hand, it is a warning that ignoring the connectivity can be misleading. On the other hand, this observation suggests a possibility to characterize a tree-like structure from ADC measurements. Importantly, we found that the distribution of branch lengths has almost no effect on D_L, thus supporting the hypothesis that D_L describes an average branch length of the dendrite trees rather than a specific distribution of the branch lengths. We found also that D_L is not affected by the branch orientation distribution, the gradient direction, and the maximal number of branches per node.

The present study relies on several assumptions and simplifications.

• Random trees were constructed in order to provide a flexibility in changing various characteristics of dendrites such as the average branch length and branch length distribution, dispersion of branch orientations, and the maximal number of branches per node. The use of synthetically constructed trees allowed us to get a reliable statistical sampling and to reveal the relative roles of these neuronal characteristics. An interesting perspective consists in applying the efficient numerical technique developed in this paper for solving the Bloch-Torrey equation on a tree, to real digitally reconstructed neurons from the NeuroMorpho.org database (see [23,25]).

• The transverse diffusivity D_T was neglected because the radius R of dendrites (below a micron) is much smaller than the diffusion length L_{diff} which ranges between 5 and 25 microns in typical dMRI experiments. In order to validate this approximation, one can estimate the signal attenuation due to restricted diffusion of water in the transverse cross-section of a cylinder in the motional narrowing regime [3,40]:

$$S_{cross} \simeq \exp\left(-bD_0 \frac{2\zeta_{-1}R^4}{D_0^2\delta(\Delta - \delta/3)}\right), \tag{23}$$

where $\zeta_{-1} = 7/96$ is a numerical factor. Setting $R = 1$ μm and $\Delta = \delta = 2.5$ ms yields a negligible signal attenuation in the transverse plane: $S_{cross} \simeq \exp(-0.002bD_0) \simeq 1$.

• Throughout this paper, we focused on the apparent diffusion coefficient as a source of information about the dendrite tree, and thus discarded additional information that could potentially be inferred from the whole dependence of the dMRI signal on b-value. This simplification is applicable to arbitrary confining domain and it does not require any *a priori* fitting model for the

dMRI signal. The analysis of dMRI signals from dendrite trees instead of their ADCs presents another perspective of this study. These signals, which are easily computable for an arbitrary tree structure, and their non-Gaussian features can provide further information on neuronal microstructure [1–4,41–43].

• Yet another important point is that we focused on the dMRI signal uniquely from *isolated* dendrite trees. The first extension of the model can consist in including the signal from the extra-cellular space. Since the extra-cellular space cannot be decomposed into simple structural elements (as we did for the dendrite tree which was decomposed into one-dimensional segments), one would need to solve the Bloch-Torrey equation over the whole (sub)-voxel in order to compute the related signal. Other constituents of the brain tissue (such as glial cells) can also be included. Although such a computation is feasible on a small sub-voxel domain (e.g., by using a finite element method developed in [34]), this problem is much more computationally demanding. In a first approximation, one could treat the extra-cellular space as a Gaussian pool with a reduced effective diffusion coefficient (see [20]). In the next step, one can attempt to account for the diffusive exchange between the dendrite tree and the extra-cellular space. In this case, one would need to solve the coupled Bloch-Torrey equations for the interior and exterior compartments in three dimensions. This is a challenging numerical problem for a realistic tissue microstructure. In turn, our simplified model allows for rapid numerical solution of essentially one-dimensional Bloch-Torrey equation on large samples of real or randomly generated synthetic dendrite trees.

5. Conclusion

We numerically studied a cylinder model of the dMRI signal in brain tissue, which relies on a longitudinal diffusivity D_L in the neurites. Using a least squares fit of the cylinder model to the ADC_0 from synthetically generated dMRI signals, we analyzed how the dendrite tree structure affects the value and the quality of the fit for the longitudinal diffusivity. We found that D_L depends on the ratio between the average branch length and the diffusion length. When the dendrite branches are short compared to the diffusion length, D_L varies significantly with the diffusion time. On the other hand, D_L has very weak dependence on branch orientation and branch length distributions and on the number of branches per node. We conclude that the cylinder model which ignores the dendrite tree connectivity, can still be a useful description of the ADC_0 in brain tissue.

Acknowledgment

This work was funded in part by the Agence Nationale de la Recherche project "SIMUDMRI". We acknowledge numerous constructive remarks from the reviewers.

Appendix A. Algorithm for generating random dendrite trees

For $i = 1, 2, \ldots, W$

1. Choose the number of branches, $\mathcal{K}$ (fixed at a prescribed value or chosen randomly, to be specified).
2. Choose randomly the $\mathcal{K}$ branch orientations: $\{\mathbf{e}_1, \ldots, \mathbf{e}_{\mathcal{K}}\}$ (unit vectors in $\mathbb{R}^3$), from a uniform distribution in the spherical cap of the unit sphere that satisfies $0 \leqslant \phi \leqslant \phi_{\max}$, where ϕ is the angle with respect to the z-axis. We restrict $\phi_{\max} \leqslant \pi/2$ to ensure that the dendrite tree always grows up. By default, we set $\phi_{\max} = \pi/2$ (unless another choice is explicitly specified).
3. Choose the branch lengths, $\ell_1, \ldots, \ell_{\mathcal{K}}$ (fixed at a prescribed value or chosen randomly, to be specified).
4. The first node of the tree is always at the origin: $\mathbf{v}_0 = (0, 0, 0)$. For the current set of nodes $\{\mathbf{v}_0, \ldots, \mathbf{v}_{k-1}\}$, we add a new branch by choosing a node $\mathbf{v}$ randomly from $\{\mathbf{v}_0, \ldots, \mathbf{v}_{k-1}\}$. Then $\mathcal{T}_k \equiv \{\mathbf{v} + s\mathbf{e}_k, s \in [0, \ell_k]\}$ is a new branch of the tree and $\mathbf{v}_k \equiv \mathbf{v} + \ell_k \mathbf{e}_k$ is a new node (added to the list). The maximum number of branches at each node is limited to be $J_{\max}$ (i.e., if the chosen node $\mathbf{v}$ has $J_{\max}$ branches, it is ignored, and the selection is repeated until the chosen node has less than $J_{\max}$ branches). This iterative construction is repeated $\mathcal{K}$ times to produce $\mathcal{K}$ branches $\mathcal{T}_1, \ldots, \mathcal{T}_{\mathcal{K}}$ and $\mathcal{K} + 1$ nodes $\mathbf{v}_0, \ldots, \mathbf{v}_{\mathcal{K}}$.
5. Define the tree $\mathcal{N}^i \equiv \bigcup_{k=1}^{\mathcal{K}} \mathcal{T}_k$.

End For.

Appendix B. Randomly oriented isolated branches of finite length

For a single isolated infinitely thin branch of length ℓ, the Gaussian phase approximation yields the dMRI signal for a standard PGSE sequence with two rectangular gradient pulses as [3]

$$S = \exp\left(-b\cos^2(\beta) D_L(D_0\Delta/\ell^2, D_0\delta/\ell^2)\right), \tag{B.1}$$

where β is the angle between the gradient and the branch directions, and the longitudinal diffusivity is

$$D_L(\tau_\Delta, \tau_\delta) = D_0 \frac{2}{\tau_\delta(\tau_\Delta - \tau_\delta/3)} \times \left[\frac{1}{120} - \frac{4}{\tau_\delta}\sum_{m=1}^{\infty} \frac{2 + e^{-(\tau_\Delta+\tau_\delta)\lambda_m} + e^{-(\tau_\Delta-\tau_\delta)\lambda_m} - 2e^{-\tau_\Delta\lambda_m} - 2e^{-\tau_\delta\lambda_m}}{\lambda_m^4}\right], \tag{B.2}$$

with $\lambda_m = \pi^2(2m-1)^2$. While the signal representation (B.1) is an approximation (valid for small b-values), Eq. (B.2) for D_L is exact. In the long length limit $\ell \to \infty, D_L(\tau_\Delta, \tau_\delta)$ approaches D_0, as expected. In the opposite short length limit $\ell \to 0$, the sum can be neglected (as compared to $1/120$) yielding $D_L \simeq \frac{\ell^4}{60 D_0 \delta(\Delta - \delta/3)}$ in the motional narrowing regime [3]. As expected, the longitudinal diffusivity vanishes in this limit.

For a large sample of randomly oriented branches of random lengths, the total dMRI signal is obtained by summing weighted contributions from all branches. If the probability density $Q_b(\theta, \phi)$ for branch orientations is independent from the probability density $p(\ell)$ for branch lengths, one retrieves Eq. (5) for ADC_0 with the longitudinal diffusivity D_L averaged over the distribution of branch lengths:

$$D_L = \int d\ell p(\ell) D_L(D_0\Delta/\ell^2, D_0\delta/\ell^2). \tag{B.3}$$

This diffusivity depends on the diffusion time Δ and on the gradient pulse duration δ (the latter dependence being weak if the branch length ℓ is greater than $\sqrt{D_0\delta}$).

References

[1] D.S. Tuch, T.G. Reese, M.R. Wiegell, V.J. Wedeen, Diffusion MRI of complex neural architecture, Neuron 40 (2003) 885–895.
[2] J. Frahm, P. Dechent, J. Baudewig, K.D. Merboldt, Advances in functional MRI of the human brain, Prog. Nucl. Magn. Reson. Spectr. 44 (2004) 1–32.
[3] D.S. Grebenkov, NMR survey of reflected Brownian motion, Rev. Mod. Phys. 79 (2007) 1077–1137.
[4] D. Le Bihan, H. Johansen-Berg, Diffusion MRI at 25: exploring brain tissue structure and function, NeuroImage 61 (2012) 324–341.
[5] A. Szafer, J. Zhong, J.C. Gore, Theoretical model for water diffusion in tissues, Magn. Reson. Med. 33 (1995) 697–712.
[6] G.J. Stanisz, A. Szafer, G.A. Wright, R.M. Henkelman, An analytical model of restricted diffusion in bovine optic nerve, Magn. Reson. Med. 37 (1997) 103–111.

[7] Y. Assaf, R.Z. Freidlin, G.K. Rohde, P.J. Basser, New modeling and experimental framework to characterize hindered and restricted water diffusion in brain white matter, Magn. Reson. Med. 52 (2004) 965–978.
[8] C.D. Kroenke, J.J.H. Ackerman, D.A. Yablonskiy, On the nature of the NAA diffusion attenuated MR signal in the central nervous system, Magn. Reson. Med. 52 (2004) 1052–1059.
[9] P.N. Sen, P.J. Basser, Modeling diffusion in white matter in the brain: a composite porous medium, Magn. Reson. Imaging 23 (2005) 215–220.
[10] H. Zhang, P.L. Hubbard, G.J.M. Parker, D.C. Alexander, Axon diameter mapping in the presence of orientation dispersion with diffusion MRI, NeuroImage 56 (2011) 1301–1315.
[11] H. Zhang, T. Schneider, C.A. Wheeler-Kingshott, D.C. Alexander, NODDI: practical in vivo neurite orientation dispersion and density imaging of the human brain, NeuroImage 61 (2012) 1000–1016.
[12] W.S. Price, A.V. Barzykin, K. Hayamizu, M. Tachiya, A model for diffusive transport through a spherical interface probed by pulsed-field gradient NMR, Biophys. J. 74 (1998) 2259–2271.
[13] D.S. Grebenkov, Pulsed-gradient spin-echo monitoring of restricted diffusion in multilayered structures, J. Magn. Reson. 205 (2010) 181–195.
[14] M.D. Budde, J.A. Frank, Neurite beading is sufficient to decrease the apparent diffusion coefficient after ischemic stroke, Proc. Nat. Ac. Sci. USA 107 (2010) 14472–14477.
[15] D.S. Novikov, E. Fieremans, J.H. Jensen, J.A. Helpern, Random walks with barriers, Nat. Phys. 7 (2011) 508–514.
[16] D.S. Novikov, J.H. Jensen, J.A. Helpern, E. Fieremans, Revealing mesoscopic structural universality with diffusion, Proc. Nat. Ac. Sci. USA 111 (2014) 5088–5093.
[17] D.A. Yablonskiy, A.L. Sukstanskii, Theoretical models of the diffusion weighted MR signal, NMR Biomed. 23 (2010) 661–681.
[18] P.T. Callaghan, Principles of Nuclear Magnetic Resonance Microscopy, Clarendon Press, Oxford, 1991.
[19] D.A. Yablonskiy, A.L. Sukstanskii, J.C. Leawoods, D.S. Gierada, G.L. Bretthorst, S.S. Lefrak, J.D. Cooper, M.S. Conradi, Quantitative in vivo assessment of lung microstructure at the alveolar level with hyperpolarized 3He diffusion MRI, Proc. Nat. Ac. Sci. USA 99 (2002) 3111–3116.
[20] S.N. Jespersen, C.D. Kroenke, L. Østergaard, J.J.H. Ackerman, D.A. Yablonskiy, Modeling dendrite density from magnetic resonance diffusion measurements, NeuroImage 34 (2007) 1473–1486.
[21] S.N. Jespersen, C.R. Bjarkam, J.R. Nyengaard, M.M. Chakravarty, B. Hansen, T. Vosegaard, L. Østergaard, D.A. Yablonskiy, N.C. Nielsen, P. Vestergaard-Poulsen, Neurite density from magnetic resonance diffusion measurements at ultrahigh field: comparison with light microscopy and electron microscopy, NeuroImage 49 (2010) 205–216.
[22] S.N. Jespersen, L.A. Leigland, A. Cornea, C.D. Kroenke, Determination of axonal and dendritic orientation distributions within the developing cerebral cortex by diffusion tensor imaging, IEEE Trans. Med. Imaging 31 (2012) 16–32.
[23] M.B. Hansen, S.N. Jespersen, L.A. Leigland, C.D. Kroenke, Using diffusion anisotropy to characterize neuronal morphology in gray matter: the orientation distribution of axons and dendrites in the NeuroMorpho.org database, Front. Integr. Neurosci. 14 (7) (2013) 31.
[24] J.E. Tanner, E.O. Stejskal, Restricted self-diffusion of protons in colloidal systems by the pulsed-gradient, spin-echo method, J. Chem. Phys. 49 (1968) 1768–1777.
[25] Details and references on NeuroMorpho database are provided at <www.neuromorpho.org>.
[26] D.S. Grebenkov, G. Guillot, B. Sapoval, Restricted diffusion in a model acinar labyrinth by NMR: theoretical and numerical results, J. Magn. Reson. 184 (2007) 143–156.
[27] J. Parra-Robles, J.M. Wild, The influence of lung airways branching structure and diffusion time on measurements and models of short-range 3He gas MR diffusion, J. Magn. Reson. 225 (2012) 102–113.
[28] H.L. Seldon, Structure of human auditory cortex. III: statistical analysis of dendritic trees, Brain Res. 249 (1982) 211–221.
[29] H. Duan, S.L. Wearne, J.H. Morrison, P.R. Hof, Quantitative analysis of the dendritic morphology of corticocortical projection neurons in the macaque monkey association cortex, Neuroscience 114 (2002) 349–359.
[30] C. Bielza, R. Benavides-Piccione, P. López-Cruz, P. Larrañaga, J. DeFelipe, Branching angles of pyramidal cell dendrites follow common geometrical design principles in different cortical areas, Scient. Rep. 4 (2014) 5909.
[31] P.C. Bressloff, V.M. Dwyer, M.J. Kearney, A 'sum-over-paths' approach to diffusion on trees, J. Phys. A: Math. Gen. 29 (1996) 1881.
[32] D.S. Grebenkov, M. Filoche, B. Sapoval, M. Felici, Diffusion-reaction in branched structures: theory and application to the lung acinus, Phys. Rev. Lett. 94 (2005) 050602.
[33] A.L. Sukstanskii, J.D. Quirk, D.A. Yablonskiy, Probing lung microstructure with hyperpolarized 3He gradient echo MRI, NMR Biomed. 27 (2014) 1451–1460.
[34] D.V. Nguyen, J.-R. Li, D.S. Grebenkov, D. Le Bihan, An efficient finite-elements code to simulate diffusion MRI signals in complex tissue geometries, J. Comput. Phys. 263 (2014) 283–302.
[35] A.M. Mastro, M.A. Babich, W.D. Taylor, A.D. Keith, Diffusion of a small molecule in the cytoplasm of mammalian cells, Proc. Nat. Acad. Sci. USA 81 (1984) 3414–3418.
[36] K. Fushimi, A.S. Verkman, Low viscosity in the acqueous domain of cell cytoplasm measured by picosecond polarization microfluorometry, J. Cell. Biol. 112 (1991) 719–725.
[37] H.J. Laubach, P.M. Jakob, K.O. Loevblad, A.E. Baird, M.P. Bovo, R.R. Edelman, S.W. Warach, A phantom for diffusion-weighted imaging of acute stroke, J. Magn. Reson. Imaging 8 (1998) 1349–1354.
[38] R. Nicolas, F. Aubry, J. Pariente, X. Franceries, N. Chauveau, L. Saint-Aubert, F. Chollet, S. Breil, P. Celsis, Water diffusion in q-space imaging as a probe of cell local viscosity and anomalous diffusion in grey and white matter, Diff. Fundam. 14 (2010) 3.
[39] I. Lavdas, K.C. Behan, A. Papadaki, D.W. McRobbie, E.O. Aboagye, A phantom for diffusion-weighted MRI, J. Magn. Reson. Imaging 38 (2013) 173–179.
[40] C.H. Neuman, Spin echo of spins diffusion in a bounded medium, J. Chem. Phys. 60 (1974) 4508–4511.
[41] J.H. Jensen, J.A. Helpern, A. Ramani, H. Lu, K. Kaczynski, Diffusional kurtosis imaging: the quantification of non-Gaussian water diffusion by means of magnetic resonance imaging, Magn. Reson. Med. 53 (2005) 1432–1440.
[42] V.G. Kiselev, The cumulant expansion: an overarching mathematical framework for understanding diffusion NMR, in: D.K. Jones (Ed.), Diffusion MRI: Theory, Methods, and Applications, Oxford University Press, Oxford, 2011, pp. 152–168.
[43] D.S. Grebenkov, Exploring diffusion across permeable barriers at high gradients. II: localization regime, J. Magn. Reson. 248 (2014) 164–176.